Soft Matter

ROYAL SOCIETY OF CHEMISTRY

PAPER

View Article Online
View Journal | View Issue

Cite this: *Soft Matter*, 2020, **16**, 6115

How do chemical patterns affect equilibrium droplet shapes?†

Yanchen Wu, *[a] Fei Wang,*[a] Shaoping Ma,[a] Michael Selzer[ab] and Britta Nestler[ab]

Received 3rd February 2020,
Accepted 26th May 2020

DOI: 10.1039/d0sm00196a

rsc.li/soft-matter-journal

By utilizing a proposed analytical model in combination with the phase-field method, we present a comprehensive study on the effect of chemical patterns on equilibrium droplet morphologies. Here, three influencing factors, the droplet sizes, contact angles, and the ratios of the hydrophilic area to the hydrophobic area, are contemplated. In the analytical model, chemical heterogeneities are described by different non-linear functions. By tuning these functions and the related parameters, the analytical model is capable of calculating the energy landscapes of the system. The chemically patterned surfaces display complex energy landscapes with chemical-heterogeneity-induced local minima, which correspond to the equilibrium morphologies of the droplets. Phase-field (PF) simulations are accordingly conducted and compared with the predicted equilibrium morphologies. In addition, we propose a modified Cassie–Baxter (CB) model to delineate the equilibrium droplet shapes. In contrast to the classic CB model, our extension is not only restricted to the shape with a spherical cap. Both the energy landscape method and the modified CB model are demonstrated to have a good agreement with the PF simulations.

1 Introduction

Predicting the droplet shapes and manipulating the movement of droplets on heterogeneous surfaces have sparked great interest both in fundamental research and industrial applications. For instance, the precise deposition of droplets with controlled shapes is of significance in liquid-based printing applications, such as inkjet printing,[1,2] surface tension induced microfluidic devices,[3,4] lab-on-a-chip,[5,6] manipulation of the interactions in protein adsorption,[7,8] liquid metal printing,[9] solder droplet printing,[10] and droplet sampling.[11,12] Diverse strategies have been applied to regulate the droplet shapes, among which chemical pattern and surface geometry methods are widely utilized.[13–17] Taking droplet sampling for example, a superhydrophilic–superhydrophobic patterned surface can be used to form arrays of droplets where active molecules, nonadherent cells, or microorganisms are trapped for high-throughput (HT) screening.[11,12] Moreover, through careful design of the patterned surface, we can obtain the desired droplet shapes with a certain size, within which biochemical reactions occur, and the shape and size of the droplets can influence the reaction process. These patterned surfaces ranging from millimeter scale to nanometer scale are obtained by using printed circuit board technology, elastomer stamps, photolithography, and lithography, to name a few.[18] In this study, we use a versatile and robust strategy to show a complete control of droplet shape *via* the design of chemical patterns. We anticipate that this liquid-based patterning strategy will facilitate droplet manipulation technology.

Droplets on chemically patterned surfaces may have multiple equilibrium shapes, which are caused by the pinning effect on the surface discontinuity.[19] The equilibrium shape of a sessile droplet is obtained by minimizing its total interfacial energy. At the equilibrium state, the droplet has a constant mean curvature, which is governed by the Young–Laplace equation. The local contact angle is determined by the three surface tensions on the triple line, which follows the quintessential Young's law. When droplets are deposited on a heterogeneous surface, the classical Cassie–Baxter model (CB) has been proven to be a successful model in a wide range of situations.[20–23] However, this model can merely predict the apparent contact angle of droplets on a composite surface and loses its validity when the wavelength of the roughness or chemical heterogeneity is relatively large.[24] To extend and amend the CB model, different modified approaches have been proposed and discussed.[23,25–30] Carmeliet *et al.* studied droplet wetting and distortion on chessboard-patterned surfaces with varying patch sizes. They found a critical ratio of the patch size to the droplet radius, above which the droplet shape is distorted and no single contact angle can be determined. When the chemical heterogeneity is

[a] *Institute of Applied Materials-Computational Materials Science, Karlsruhe Institute of Technology, Straße am Forum 7, 76131 Karlsruhe, Germany. E-mail: yanchen.wu@kit.edu, fei.wang@kit.edu*
[b] *Institute of Digital Materials Science, Karlsruhe University of Applied Sciences, Moltkestraße 30, 76133 Karlsruhe, Germany*

† Electronic supplementary information (ESI) available. See DOI: 10.1039/d0sm00196a

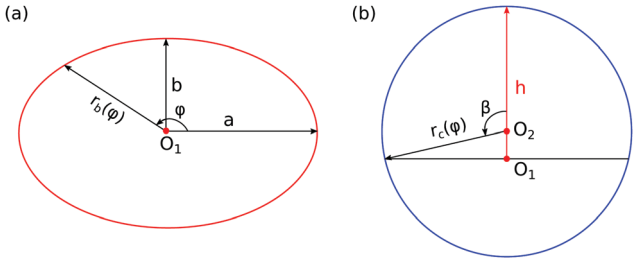

Fig. 1 Schematic illustration for the geometric assumptions of a droplet on a chemically patterned surface. (a) Bottom view. The red ellipse centred at O_1 with semi-axes a and b is the droplet baseline. The parameter r_b denotes the base radius. (b) Side view. The circular arc above the black line passing through O_1 corresponds to a circle centred at O_2 with radius r_c and depicts the profile of the liquid–gas interface. Here, h is the droplet height, and φ and β represent polar angles on the surfaces of the red ellipse and blue arc, respectively.

comparable to the droplet size, anisotropic wetting may happen and the complex geometry of the deformed droplet is challenging to describe with a general analytical method. One common method to delineate static anisotropic wetting for droplets on chemically heterogeneous surfaces is studying droplet distortion from the baseline, since the baseline profile of the droplet is more accurate, symmetric, and stable.[31] Here, the droplet distortion is quantified by the ratio a/b, where a and b are the lengths of the half major and minor axis of the droplet baseline (see Fig. 1(a)). The anisotropic droplet shapes on chemically patterned surfaces have been investigated by a number of authors.[18,32–47]

Due to the lack of accurate prediction of the number as well as the shapes of equilibrated droplets on chemically patterned surfaces, the elaborate maneuver of droplet formation and morphology control remains a tough task. In this work, we show that the equilibrium shapes of droplets on chemically patterned surfaces can be analytically predicted by minimizing the free energy of the system. A free energy minimization method has been previously used in ref. 18 to study the morphological transitions of droplet states with a variation in the droplet volumes and the contact angles on striped patterned surfaces. They theoretically derived stability criteria for the morphological transitions of droplets on striped surfaces by using simple parameterizations of the channels and bulges in terms of cylindrical and spherical segments. Differing from this purpose, the present model aims to find the complete set of equilibrium states, where more complex patterned surfaces are considered. For this consideration, we use a concise model, where the baseline of the droplets is approximately delineated by an ellipse with semi-axes a and b. Benefiting from this approximation, we are able to calculate the total interfacial energy by integration and thus obtain the energy landscapes in terms of a and b. Here, a and b are used to identify different local energy minima and the corresponding equilibrium shapes of droplets. Our prediction is based on the surface energy landscapes and all the energy minima are checked through phase-field simulations. By using both methods together, we address the complete set of equilibrium states of droplets. Moreover, we propose a modified CB model to compare with the diverse predicted equilibrium droplet shapes. We further elucidate that the number and the shapes of the equilibrated droplets can be controlled by tuning the droplet sizes, contact angles, and the ratios of the hydrophilic to the hydrophobic areas. We emphasize that we herein focus on droplets whose size is comparable to the length scale of the chemical patterns, both of which are smaller than the capillary length, so that the influence of gravity can be neglected.

Simulation offers great flexibility and efficiency in investigating droplet wetting phenomena under various conditions and thus sometimes shows great advantages over experiments. Various numerical methods have been devoted to modeling droplet behaviors, like molecular dynamics (MD) and Monte Carlo (MC) methods, the Lattice-Boltzmann method (LB), thin-film model, and phase-field method (PF), to name a few. Among these methods, the MD and MC methods are usually restricted to the nano- or microscale owing to the relatively high computational load. The LB method and the thin-film model are applicable at the mesoscale. The LB method with a scale-bridging nature shows a great advantage in the parallel implenentation and the simplicity of programming,[48] yet it usually suffers from the shortcoming of high spurious velocities at the interface.[49] As derived by a long wave approximation from the Navier–Stokes equations to a single nonlinear partial differential equation for the film thickness, the thin-film model can be used to simplify some fluid dynamics problems.[50,51] Actually, the thin-film model includes a form of the Cahn–Hilliard equation and thus describes the dynamics of a conserved order parameter field.[52,53] The Cahn–Hilliard type PF model and Allen–Cahn type PF model both can be viewed as the gradient flow of the Lyapunov energy functional and thus show a monotonic decrease in the total free energy with time.[54] Since the Cahn–Hilliard type PF model is naturally conserved, *i.e.*, the mass conservation is obeyed, the dynamic process of the described system can be taken into account. This makes it possible to conduct an analysis of instability phenomena like spinodal dewetting, Rayleigh instability, *etc.*[55–57] However, the Allen–Cahn type PF model can be considered as a gradient dynamics, and its kinetic path is different from the Cahn–Hilliard type model. In this work, we use an Allen–Cahn type PF model with volume preservation. In this model, an additional bulk energy is introduced to counterbalance the volume changes caused by the original nonlinear terms in the Allen–Cahn type PF model, similar to the role of a Lagrange multiplier to ensure volume conservation. The idea can be seen as some kind of redistribution of mass along the corresponding phase boundaries.[58] Compared to the Cahn–Hilliard model, the Allen–Cahn equation is more numerically efficient, especially for three-dimensional simulations, which are necessary for the study of the chocolate and chessboard pattern surfaces in the current work. The PF model, which is a diffuse interface model, has been extensively studied and employed in the areas of large interface deformations or topological changes, such as droplet coalescence, breakup, wetting, and so forth.[59] A great advantage of the PF model is that it is free of explicitly tracking the interface between two phases, making it feasible to implement

for interfacial dynamics in multi-phase flows. More information about the advantages and limitations of the PF method have been elucidated in ref. 60.

The paper is organized as follows: we first explain the theoretical framework for describing the equilibrium shapes of droplets on different chemically patterned surfaces. Then, we introduce the numerical method, and thereafter we utilize the theoretical framework combined with numerical simulations to investigate the number and shapes of equilibrated droplets affected by droplet sizes, contact angles and the ratios of the hydrophilic to the hydrophobic areas. In the last section, a summary and conclusions are presented.

2 Analytical model

In this section, we present a detailed description for the analytical method, which was only briefly depicted in our previous work.[61] We here apply this analytical approach to scrutinize the wetting of chemically patterned surfaces with various characteristic lengths, contact angles, and ratios of the hydrophilic area to the hydrophobic one, which were not contemplated in the previous work. In comparison with the model in ref. 61, three major improvements are recounted here: (i) A new parameter λ is introduced in the nonlinear functions depicting the chemical heterogeneities of the substrate. With this new parameter, it is convenient to manipulate the ratio of the hydrophilic area to the hydrophobic area. (ii) A new parameter χ is employed to control the lattice roundness of the chocolate patterned surface. (iii) Most importantly, a modified Cassie–Baxter model is proposed here for a comparison with the analytical approach.

We consider a sessile droplet on a solid surface, which can be interpreted as a three-phase system consisting of a solid, liquid, and gas phase. The equilibrium state of this system is achieved by minimizing the total interfacial energy, which is formulated as

$$E = A_{\mathrm{lg}}\gamma_{\mathrm{lg}} + \int_{A_{\mathrm{ls}}} (\gamma_{\mathrm{ls}} - \gamma_{\mathrm{gs}})\mathrm{d}A, \tag{1}$$

where A_{lg} and A_{ls} represent the areas of the liquid–gas and liquid–solid interface, respectively. The parameters γ_{lg}, γ_{ls} and γ_{gs} denote the interfacial energy density of liquid–gas, liquid–solid and gas-solid, respectively. It is postulated that the equilibrated droplet has an elliptical baseline with semi-axes a and b (Fig. 1(a)). As sketched in Fig. 1(b), the droplet cap (liquid–gas interface) is described with a series of circular arcs having varying curvature radius

$$r_{\mathrm{c}}(\varphi) = [r_{\mathrm{b}}{}^2(\varphi) + h^2]/2h, \tag{2}$$

where r_{b}, h and φ are the base radius, droplet height and polar angle of the base ellipse, respectively. In the polar coordinate, the base radius r_{b} is given by

$$r_{\mathrm{b}}(\varphi) = \frac{ab}{\sqrt{a^2\sin^2(\varphi) + b^2\cos^2(\varphi)}}. \tag{3}$$

The volume of the droplet V_{d} follows the expression

$$V_{\mathrm{d}} = \frac{\pi}{6}h(3ab + h^2). \tag{4}$$

The area of the liquid–gas interface A_{lg} is formulated as

$$A_{\mathrm{lg}} = \int_0^{2\pi} r_{\mathrm{c}}{}^2(\varphi)(1 - \cos\beta)\mathrm{d}\varphi, \tag{5}$$

where β is the polar angle between the rays from O_2 to the apex of the cap and the baseline of the droplet (see Fig. 1(b)), reading

$$\beta = \arccos\frac{r_{\mathrm{c}}(\varphi) - h}{r_{\mathrm{c}}(\varphi)}. \tag{6}$$

From eqn (2)–(5), for a droplet with a fixed volume $V_{\mathrm{d}}(a,b,h)$, the area of the droplet cap A_{lg} can be fully described *via* a and b. Therefore, the first term of the total interfacial energy in eqn (1), namely, $E_1(a,b) := \gamma_{\mathrm{lg}}A_{\mathrm{lg}}$, has two degrees of freedom.

We consider three chemically patterned surfaces, whose chemical heterogeneities are described as $f_k(r_{\mathrm{b}},\varphi) := \gamma_{\mathrm{ls}} - \gamma_{\mathrm{gs}}$, where k = 1, 2, and 3 denote the striped, chocolate, and chessboard patterns, respectively. The functions $f_k(r_{\mathrm{b}},\varphi)$ are expressed as

$$\begin{cases} f_1 = \gamma_m + \gamma_0\tanh[\xi(\cos\delta_1 - \lambda)] \\ f_2 = \gamma_m + \gamma_0\tanh\{\xi[(\cos\delta_1 - \lambda)(\cos\delta_2 - \lambda) - \chi(\cos\delta_1 + \cos\delta_2)]\} \\ f_3 = \gamma_m + \gamma_0\tanh[\xi(\cos\delta_1 - \lambda)(\cos\delta_2 - \lambda)] \end{cases} \tag{7}$$

with $\delta_1 = (2\pi r_{\mathrm{b}}\sin\varphi + i\pi L)/L$ and $\delta_2 = (2\pi r_{\mathrm{b}}\cos\varphi + j\pi L)/L$. Here, γ_m and γ_0 are the mean surface energy density difference and the amplitude of the heterogeneity, respectively. For example, the parameter set (γ_m = 0, γ_0 = 0.5) corresponds to the situation where the static equilibrium contact angles on the hydrophilic (θ_1) and hydrophobic (θ_2) areas are 60° and 120°, respectively. The sharpness of the chemical pattern is controlled by the parameter ξ.

The index i, j = 0, ±1, ±1/2,... depicts the center point position of the droplet baseline. Fig. 2 highlights all the possible coordinates of the index, with respect to which the equilibrated droplets are symmetric on the three chemically patterned surfaces. For the striped patterned surface (Fig. 2(a)), the red points P_1 (i = ±1, ±3,...) are on the center of the hydrophilic stripes (white), while the blue points P_2 (i = 0, ±2, ±4,...) locate on the center of the hydrophobic ones (grey). For the chocolate and chessboard patterned surfaces, the droplet base center points P_1, P_2, and P_3 with the coordinates (j,i) are indicated in Fig. 2(b) and (c), respectively. It should be noticed that P_1, P_2, and P_3 are periodically distributed on the surfaces and the validation for the high symmetry property of these positions has been fully discussed in ref. 61. The characteristic length is defined as $L := L_{\mathrm{dry}} + L_{\mathrm{wet}}$, where L_{dry} and L_{wet} are the respective characteristic lengths for the hydrophobic and hydrophilic areas. For instance, L_{dry} (L_{wet}) stands for the width of a hydrophobic (hydrophilic) stripe for the striped surfaces. For the chocolate and chessboard patterns, L_{dry} and L_{wet} denote the length of the hydrophobic

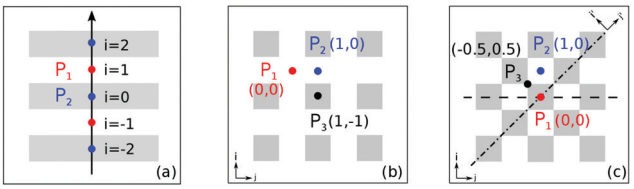

Fig. 2 (a–c) Sketches of the surface topology for three chemically patterned surfaces: stripe, "chocolate," and "chessboard." Here, the grey and white areas denote hydrophobic and hydrophilic surfaces, respectively. The coordinates of the droplet base center positions at equilibrium are highlighted by P_1, P_2 and P_3. (a) P_1: $i = 1$, P_2: $i = 0$. (b) P_1: ($j = 0$, $i = 0$), P_2: ($j = 1$, $i = 0$), and P_3: ($j = 1$, $i = -1$). (c) P_1: ($j = 0$, $i = 0$), P_2: ($j = 0$, $i = 1$), and P_3: ($j = -1/2$, $i = 1/2$) or P_1: ($j' = 0$, $i' = 0$), P_2: ($j' = 1/\sqrt{2}$, $i' = 1/\sqrt{2}$), and P_3: ($j' = 0$, $i' = 1/\sqrt{2}$). The indexes with primes for the last three points are in the rotated coordinate system.

lattice and the distance in the direction of j or i between two neighbouring hydrophobic lattices (Fig. 2(b) and (c)), respectively.

We define a parameter $\nu := L_{\mathrm{wet}}/L_{\mathrm{dry}}$ to characterize the area ratio of the hydrophilic to the hydrophobic regions on the three chemically patterned surfaces. This parameter ν is manipulated by varying λ in the functions f_1, f_2, and f_3. Here, we select three typical values of ν = 1 : 1, 1 : 2, and 1 : 3, corresponding to $\lambda = \cos 90^\circ$, $\cos 60^\circ$, and $\cos 45^\circ$, respectively. For these three values of ν, the contours $f_k(x,y)$ of the three chemically patterned surfaces are shown in Fig. 3(a)–(c), where we have made the following coordinate transformation: $x = r_{\mathrm{b}} \cos\varphi$ and $y = r_{\mathrm{b}} \sin\varphi$. It is found that the three functions with selected parameters perfectly describe the desired heterogeneity of the three typical chemically patterned surfaces. In particular, the parameter χ in f_2 is introduced to control the roundness of the isolated hydrophobic areas (red areas in Fig. 3(b)).

With the heterogeneity functions f_k, the second term of the interfacial energy in eqn (1) is calculated through the integration:

$$\int_{A_{\mathrm{ls}}} (\gamma_{\mathrm{ls}} - \gamma_{\mathrm{gs}}) \mathrm{d}A = \int_0^{2\pi} \frac{1}{2} r_{\mathrm{b}}^2 f_k(r_{\mathrm{b}}, \varphi) \mathrm{d}\varphi \cdot e \qquad (8)$$

By substituting the expressions of r_{b} in eqn (3) and $f_k(r_{\mathrm{b}},\varphi)$ in eqn (7) into eqn (8), the integration in eqn (8) depends solely on the two parameters a and b for a certain patterned surface when the droplet position is fixed, namely, $E_2(a,b) := \int_{A_{\mathrm{ls}}} (\gamma_{\mathrm{ls}} - \gamma_{\mathrm{gs}}) \mathrm{d}A$. Therefore, the total interfacial energy $E = E_1 + E_2$ can be described as a function of the parameters a and b. The philosophy of this method is to minimize the total interfacial energy E in terms of a and b, so that the equilibrium shapes of droplets are depicted by the local minima of the energy landscapes $E(a,b)$.

In the following, we will propose a modified CB model to address the equilibrated droplets on chemically patterned surfaces. Firstly, let us revisit the classical CB model, which delineates the average contact angle $\bar{\theta}$ of droplets on chemically heterogeneous surfaces:

$$\bar{\theta} = \arccos(x_1 \cos\theta_1 + x_2 \cos\theta_2). \qquad (9)$$

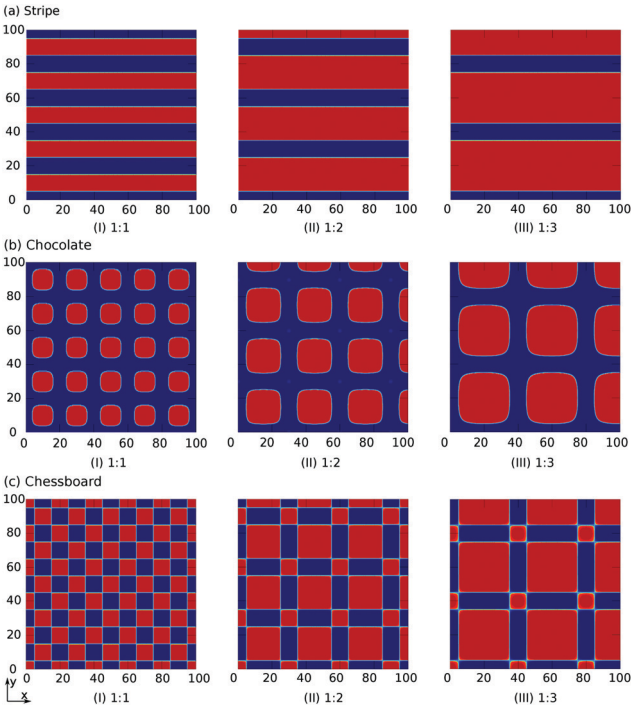

Fig. 3 (a–c) Contour plot of the functions $f_1(x,y)$, $f_2(x,y)$, $f_3(x,y)$ describing the heterogeneities of the three chemically patterned surfaces: stripe, "chocolate," and "chessboard," respectively. Here, $x = r_{\mathrm{b}} \cos\varphi$ and $y = r_{\mathrm{b}} \sin\varphi$. The patterns are obtained by setting $\gamma_m = 0$, $\gamma_0 = 0.5$, and $\xi = 100$. The characteristic length L in (I), (II), and (III) is 20, 30, and 40, respectively. The ratios ν of 1 : 1, 1 : 2, and 1 : 3 correspond to $\lambda = \cos 90^\circ$, $\cos 60^\circ$, and $\cos 45^\circ$, respectively. In (b) (I), (II), and (III), we set χ = 0.55, 0.13, and 0.10, respectively. The red and blue colors show $f_k = -0.5$ or 0.5, corresponding to the hydrophilic and hydrophobic area, respectively.

Here, x_m represents the area fraction of the surface component with the corresponding equilibrium contact angle θ_m, m = 1, 2. In the current work, the area fractions x_m range from 0.25 to 0.75. The average angle $\bar{\theta}$ actually reflects the energy minimum state of droplets and reveals the wettability of the chemically heterogeneous surface.

We assume that an equilibrated droplet on the chemically patterned surface is delineated by a spherical cap (see Fig. 4), whose contact angle reads $\bar{\theta}$. This spherical cap is described by

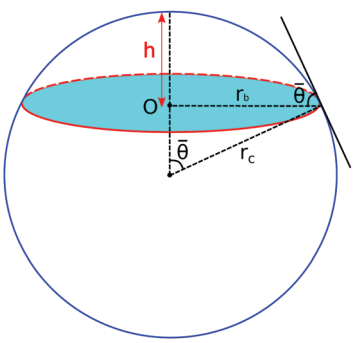

Fig. 4 Droplet morphology in the form of a spherical cap. The liquid–solid contact area is highlighted in the cyan color.

the following equations

$$\begin{cases} V_d = \pi(3r_b^2 + h^2)/6 & \text{volume} \\ h = r_c(1 - \sin\bar{\theta}) & \text{height} \\ r_b = r_c \sin\bar{\theta} & \text{base radius.} \end{cases} \quad (10)$$

Here, r_c and r_b are both constants. When the droplet volume V_d and $\bar{\theta}$ are given, r_b is obtained *via* eqn (10), namely, $r_b = r_b(V_d,\bar{\theta})$. The baseline of an equilibrated droplet may deviate from the circular shape (red circle in Fig. 4) and exhibit an elliptical morphology, as assumed in the previous section. In this case, we use the contact area $A_{sl} = \pi r_b^2$ of the circular base area as a reference value to appraise the one of the elliptical base area, *i.e.*, $\pi ab = \Psi(V_d,\bar{\theta})$, where $\Psi = \pi r_b^2$. The proposed modified CB model will be compared with the PF simulations in the following.

3 Numerical model

Mathematically, the process of a droplet depositing on a surface can be seen as a free boundary problem where the evolving interface minimizes its surface energy to achieve an energetically favourable state. In this work, an Allen–Cahn-type phase-field method is utilized to simulate the equilibrium shapes of droplets on chemically patterned surfaces. This model has been comprehensively discussed and validated in previous studies.[61–64] For brevity, we here give a succinct description of this method. To describe the liquid (l) and gas (g) phases, we introduce a space- and time-dependent order parameter $\phi(\mathbf{x},t)$ varying continuously from 0 to 1 across the liquid–gas interface. In the pure liquid and the pure gas phases, we have $\phi = 1$ and $\phi = 0$, respectively. The time evolution of the order parameter $\phi(\mathbf{x},t)$ acts to reduce the free energy functional of the system, which is formulated as[61–67]

$$\mathscr{F}(\phi) = \int_\Omega \left[\frac{1}{\varepsilon}w(\phi) + \varepsilon a(\phi,\nabla\phi) + g(\phi)\right]\mathrm{d}\Omega + \int_S f_w(\phi)\mathrm{d}S. \quad (11)$$

Here, Ω and S indicate the spatial domain and solid–fluid boundary, respectively. The parameter ε is related to the thickness of the liquid–gas interface. The function $w(\phi)$ is an obstacle potential, which reads

$$w(\phi) = \begin{cases} \frac{16}{\pi^2}\gamma_{lg}\phi(1-\phi) & \text{if } \phi \in [0,1] \\ \infty & \text{else.} \end{cases} \quad (12)$$

The term $a(\phi,\nabla\phi)$ in eqn (11) denotes the gradient energy density, which is expressed as

$$a(\phi,\nabla\phi) = \gamma_{lg}|\nabla\phi|^2. \quad (13)$$

The bulk energy density $g(\phi)$ in eqn (11) is adopted to ensure volume conservation[58,68]

$$g(\phi) = \sum_{\alpha=1}^{2} \chi_\alpha l(\phi_\alpha), \quad (14)$$

where χ_α is a weight function and $l(\phi) = \phi^3(6\phi^2 - 15\phi + 10)$ represents an interpolation function. The last term in eqn (11) presents a wall free energy, which is formulated as

$$f_w(\phi) = \gamma_{ls} + (\gamma_{gs} - \gamma_{ls})l(\phi). \quad (15)$$

The time evolution of ϕ is derived by the functional derivative of $\mathscr{F}(\phi)$, reading

$$\tau\varepsilon\frac{\partial\phi}{\partial t} = 2\varepsilon\gamma_{lg}\Delta\phi - \frac{16}{\varepsilon\pi^2}\gamma_{lg}(1-2\phi) - \frac{\partial g(\phi)}{\partial\phi} \quad \text{in } \Omega, \quad (16)$$

where τ is a temporal relaxation parameter for the gas–liquid interface. As proposed in ref. 69 and 70, the boundary condition that is consistent with Young's law follows

$$\tau_w\frac{\partial\phi}{\partial t} = 2\varepsilon\gamma_{lg}\frac{\partial\phi}{\partial n} - (\gamma_{gs} - \gamma_{ls})\frac{\partial l(\phi)}{\partial\phi} \quad \text{on } S. \quad (17)$$

Here, τ_w is a phenomenological parameter determining the deviation of the system from the equilibrium state, and n depicts the normal vector of the wall S.

To solve the equation system numerically, the finite difference method on a regular grid with an explicit Euler time scheme is applied. A fine time step is adopted according to the von Neumann stability analysis, so that the numerical stability of the simulations is guaranteed. In this work, the length x, time t, and energy E are nondimensionalized by the characteristic parameters, $x^* = 1 \times 10^{-6}$ m, $t^* = 1 \times 10^{-9}$ s, and $E^* = 1 \times 10^{-11}$ J, respectively.

4 Results and discussion

In this section, by using the analytical methods proposed in Section 2 and the PF model described in Section 3, we study the influence of droplet sizes, contact angles, and the ratios of the hydrophilic area to the hydrophobic area upon the equilibrium morphologies. Here, three typical chemically patterned surfaces, namely, striped, "chocolate," and "chessboard" patterned surfaces, are considered.

4.1 Droplet size

In this part, the contact angles on hydrophilic and hydrophobic areas are set as 60° and 120°, respectively, *i.e.*, $\theta_1 = 60°$, $\theta_2 = 120°$. The characteristic length in eqn (7) is a constant value $L = 40$. With varying the droplet volume V_d, we use the ratio R/L to characterize the effect of the droplet size on the equilibrium patterns. Here, R is the effective radius of the droplet, which is calculated according to $R = (3V_d/4\pi)^{1/3}$.

In Fig. 5, we present the surface energy landscapes for droplets with different volumes as well as the corresponding equilibrated states on the chocolate-patterned surface. For the sake of conciseness, the simulation setups, the energy maps, and the snapshots of the equilibrated droplets on the other two patterns (striped and chessboard patterned surfaces) are fully described in the ESI.† From (I) to (III) in Fig. 5, the size of the droplets varies from $R/L = 0.75$ to $R/L = 0.25$. The hydrophobic square lattices (red) have a width of $L_{dry} = L/2 = 20$ and the distance between two neighbouring lattices is $L_{wet} = L/2 = 20$.

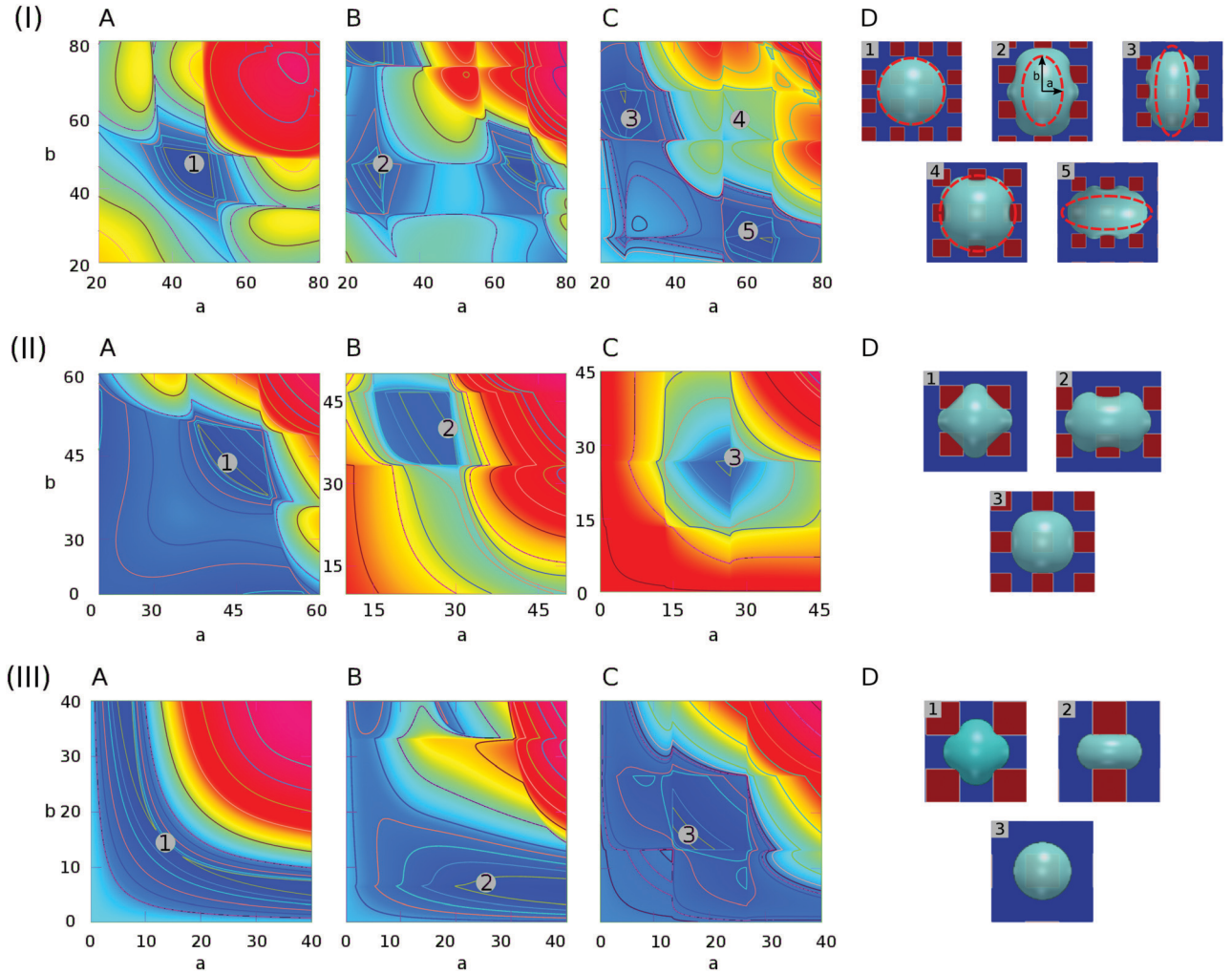

Fig. 5 Surface energy landscapes for droplets with different sizes on chocolate-patterned surfaces and snapshots of equilibrated droplets through PF simulations. (I) R/L = 0.75, (II) R/L = 0.5, and (III) R/L = 0.25. The chemical heterogeneities are described by $f_2(r_b,\varphi)$ in eqn (7) with the following parameters: γ_m = 0, γ_0 = 0.5, ξ = 100, L = 40, λ = 0, and χ = 0.55. The energy minima are specified by different numbers, corresponding to the snapshots in (D) labeled with the same number. The surface energy landscapes for (A), (B), and (C) depict the systems with the droplet base center positions on P_1, P_2, and P_3, respectively. (D) Snapshots of equilibrated droplets *via* PF simulations (blue: hydrophilic, red: hydrophobic).

In each panel, the surface energy landscapes in (A), (B), and (C) are for droplets with base center positions on P_1, P_2, and P_3, respectively. The energy minima in the deep blue region are sequentially numbered, corresponding to the snapshots of the PF simulation results labeled with the same number in (D). As an example, we compare the baseline (red dashed ellipse) of the droplets from the analytical model with the one from the PF simulations in (I)(D). The elliptic baseline with semi-axes a, b from the analytical model is obtained from the coordinates of the energy minima in the energy landscapes.

It is observed that the analytical predictions of the energy landscapes show satisfactory agreement with the simulation results. Actually, the elliptical baseline can be considered as an average approximation for the curved triple line of the droplets. This model is more accurate when the aspect ratio a/b is closer to 1. This can be confirmed by the fact that the first and fourth snapshots from PF simulations in (I)(D) agree excellently with the analytical model (red dashed lines), while the other snapshots with a/b far away from 1 show relatively large deviations from the analytical predictions.

Through the energy-map method and the PF simulations, we obtained the influence of the droplet size on the quantity N and the morphologies of the equilibrated droplets on the three typical chemically patterned surfaces, as illustrated in Fig. 6. Here, the top ((a), (b)), medium ((c), (d)), and bottom ((e), (f)) rows correspond to the striped, chocolate-patterned, and chessboard-patterned surfaces, respectively. As shown in Fig. 6(a), (c) and (e), the equilibrated quantity N increases with the ratio R/L. This reveals that large droplets tend to have more equilibrium shapes for all three patterned surfaces. Moreover, a comparison among Fig. 6(a), (c) and (e) shows that for a fixed ratio R/L, the number of equilibrium states increases with an increase in the complexity of the surface pattern, *i.e.*, striped-patterned surface → chocolate-patterned surface → chessboard-patterned surface. The underlying reason for the effect of the droplet volume and the complexity of the patterned

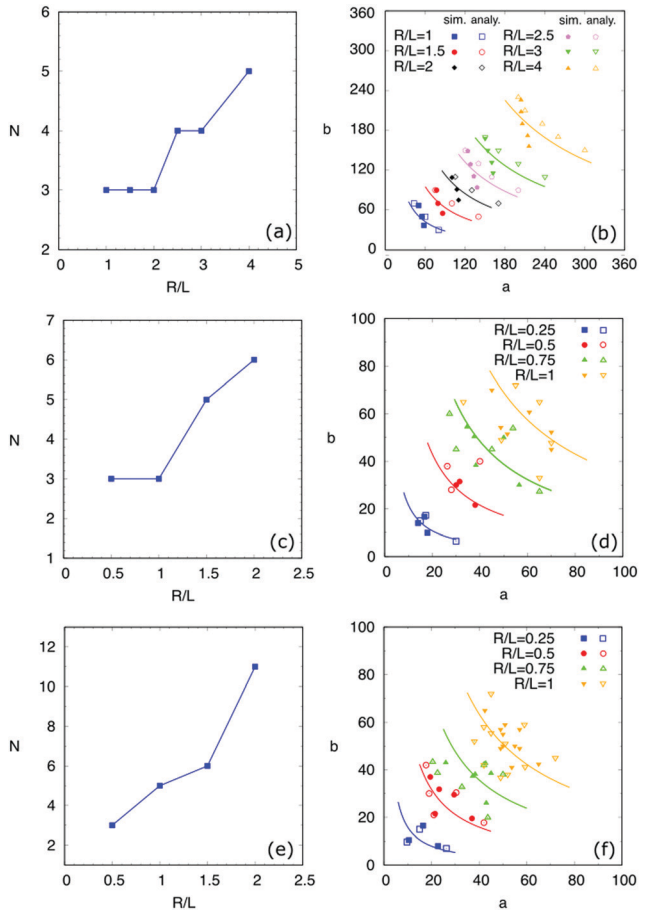

Fig. 6 The number N and the morphologies of the equilibrated droplets on three typical chemically patterned surfaces in dependence of the droplet sizes. (a and b), (c and d), and (eand f) are for striped, chocolate-patterned, and chessboard-patterned surfaces, respectively. (a), (c), and (e) depict the relation N *versus* R/L. (b), (d), and (f) describe the equilibrated droplet morphologies with different sizes predicted by PF simulations (filled symbols), in comparison with the energy-map model (hollow symbols) and the modified CB model (solid curves).

surfaces is as follows. An increase in the droplet volume and the complexity of the patterned surfaces both gives rise to more covered energy discontinuous lines, which have a pinning effect on the spreading of the droplets. Due to this pinning effect from the increased amount of discontinuous lines, more possible equilibrated droplet shapes are prone to appear.

Fig. 6(b), (d) and (f) depict the droplet base radii a and b at equilibrium from PF simulations (filled symbols) and the energy-map model (hollow symbols) in comparison with the modified CB model (solid curves). The scenarios for droplets with different sizes are distinguished by different colors. As we can see, for each volume, the simulation results coincide with the one from the energy-map model. Besides, the coloured solid curves are consistent with the same coloured symbols. Certain deviations of the energy-map model from the PF simulations are due to the strongly curved contact line of the droplets, which is caused by the pinning effect on the hydrophilic–hydrophobic discontinuous lines on the surfaces. While in our energy-map model, we have applied an elliptical baseline to averagely describe the triple line. Nevertheless, the good agreement between the simulations, energy landscape method, and the modified CB model implies the capability as well as the justifiability of the proposed approaches. It should be noticed that in the present work, there exists a limit for the aspect ratio a/b. When the value of a/b is beyond the limit, the droplet becomes slender with a super high/low aspect ratio. In this case, interfacial instabilities may appear, leading to the breakup of the droplets. This topic is out of the scope of the present study and will be addressed in forthcoming work.

At this point, we have benchmarked the analytical model by studying the number and the shapes of the equilibrated droplets with various volumes on the three typical chemically patterned surfaces. As the droplet volume increases, for a certain patterned surface, more equilibrated droplet shapes appear. In the modified CB model, we assume that the different equilibrated droplets with the same volume on a certain surface tend to have the same liquid–solid contact area. This hypothesis has been confirmed by PF simulations. For instance, as shown in Fig. 6(b), (d) and (f), for each droplet size, the results from the PF simulations and the energy landscape method (filled and hollow symbols) locate near the corresponding curve πab = constant. This reveals that the equilibrated droplets have approximately the same contact area $A_{ls} = \pi ab$. The slight deviation of the symbols from the solid curves is by dint of the disparity between the curved contact line in simulations and the postulated elliptical baseline in the analytical model. Furthermore, the distinct droplet shapes on the chemically patterned surfaces are attributed to the pinning effect on the hydrophilic/hydrophobic boundaries. Big droplets have large contact areas and long contact lines, which cross more hydrophilic/hydrophobic boundaries, leading to an increase in the number of equilibrium shapes.

4.2 Contact angle

In this section, we systematically investigate the equilibrated droplet shapes affected by the contact angles on hydrophilic and hydrophobic areas. The difference between the contact angles $\Delta\theta := \theta_2 - \theta_1$ is divided into three groups: $\Delta\theta = 30^\circ$, 45°, and 60°. As listed in Table 1, in each group, four pairs of contact angles (θ_1,θ_2) are chosen. In the following simulations, the blue and the red areas of the substrates correspond to the low contact angle (θ_1) and the high contact angle (θ_2), respectively. The characteristic length is constant $L = 40$. Droplets with the same size $(R/L = 1)$ on three typical chemically patterned surfaces are focused on.

As three typical examples, Fig. 7(I), (II) and (III) display the surface energy landscapes and the snapshots of the simulated

Table 1 The setup of contact angles

$\Delta\theta$	30°	45°	60°
Contact angle pairs (θ_1,θ_2)	$(30^\circ,60^\circ)$ $(60^\circ,90^\circ)$ $(90^\circ,120^\circ)$ $(120^\circ,150^\circ)$	$(45^\circ,90^\circ)$ $(75^\circ,120^\circ)$ $(90^\circ,135^\circ)$ $(135^\circ,180^\circ)$	$(30^\circ,90^\circ)$ $(60^\circ,120^\circ)$ $(90^\circ,150^\circ)$ $(120^\circ,180^\circ)$

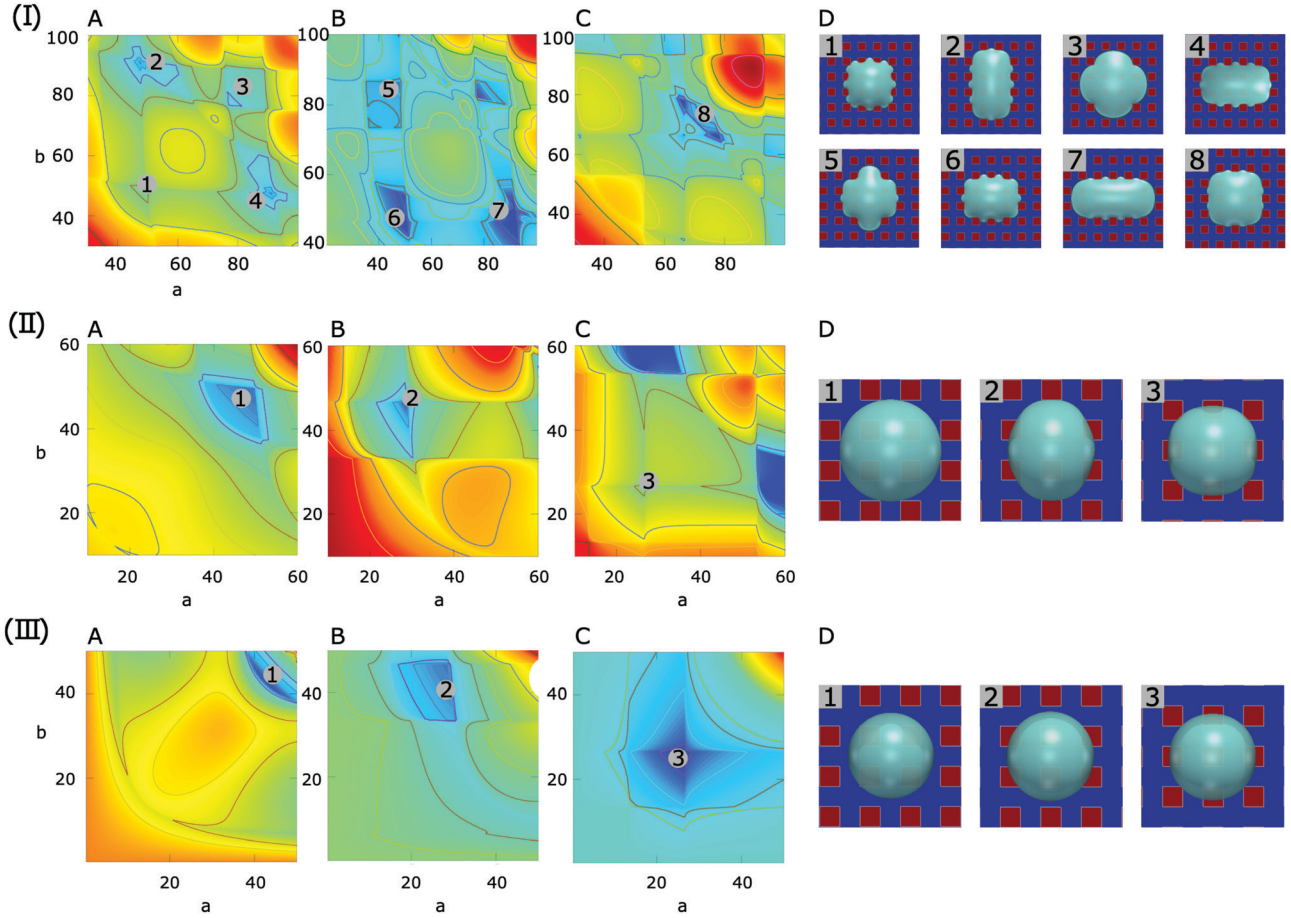

Fig. 7 Surface energy landscapes for droplets on chocolate-patterned surfaces with different contact angles and corresponding snapshots of equilibrated droplets from PF simulations. (I) $\theta_1 = 30^\circ$, $\theta_2 = 90^\circ$, (II) $\theta_1 = 90^\circ$, $\theta_2 = 150^\circ$, and (III) $\theta_1 = 120^\circ$, $\theta_2 = 180^\circ$. The chemical heterogeneities are depicted by $f_1(r_b,\varphi)$ in eqn (7) with $\xi = 100$, $L = 40$, $\lambda = 0$, and $\chi = 0.55$. The mean value γ_m and the amplitude γ_0 of the surface energy density are set according to the contact angle pairs. The energy minima are shown by different numbers, corresponding to the snapshots in (C) labeled with the same number. The surface energy landscapes for (A), (B) and (C) represent the setups where the droplet base center positions are P_1, P_2 and P_3, respectively. (D) Snapshots of equilibrated droplets from PF simulations (blue: hydrophilic, red: hydrophobic).

equilibrium droplets on the chocolate-patterned surface for contact angle pairs (30°, 90°), (90°, 150°), (120°, 180°), respectively. The surface energy landscapes (A), (B), and (C) in each panel correspond to droplets with base centers locating on P_1, P_2, and P_3, respectively. The energy minima in the energy maps are labeled with different numbers, corresponding to the simulation snapshots indicated by the same number in (D). The geometrical parameters for the patterned surface are the same as the ones in Fig. 5. For brevity, the energy landscapes and the snapshots of the equilibrated droplet shapes for striped and chessboard patterned surfaces are included in the ESI.†

By using the above-mentioned energy landscape model together with PF simulations, we found all the possible equilibrium droplet shapes on the three chemically patterned surfaces for the contact angle pairs tabulated in Table 1. The number N of the equilibrium droplet shapes *versus* $\bar{\theta}$ and $\Delta\theta$ is illustrated in Fig. 8(a), (d), (g) and (b), (e), (h), respectively. Here, the first, second, and last row correspond to the striped, chocolate, and chessboard patterned surfaces, respectively. For the three patterned surfaces, the following similarities (i) and (ii) and differences (iii) are observed: (i) For all three surfaces, N decreases with $\bar{\theta}$ and remains almost constant when $\bar{\theta} \gtrsim 100^\circ$. For instance, for the chocolate-patterned surface (Fig. 8(d)) and $\bar{\theta} \geq 100^\circ$, we observe $N = 3$ and these three states are shown in Fig. 7(II) and (III), where the droplet base centers locate at the positions P_1, P_2, and P_3, respectively. With a decrease in $\bar{\theta}$, the energy landscape becomes more intricate (see *e.g.*, Fig. 7(I)), where the quantity of equilibrium states rises. The underling reason is that with a decrease in $\bar{\theta}$, the liquid–solid contact area is enlarged, which leads to more discontinuous lines covered by the droplets. Hence, N increases with a decrease in $\bar{\theta}$. (ii) For all three patterned surfaces, N increases with a decrease in $\Delta\theta$ when $\Delta\theta < 0$. This is because when $\Delta\theta < 0$ deviates farther from 0, on the one hand, the pinning effect is more pronounced, and on the other hand, $\bar{\theta}$ decreases. (iii) Different results are observed for distinct patterned surfaces when $\Delta\theta > 0$. For the striped and chocolate patterned surfaces, N remains constant, whereas N increases with $\Delta\theta$ for the chessboard patterned surface. The former

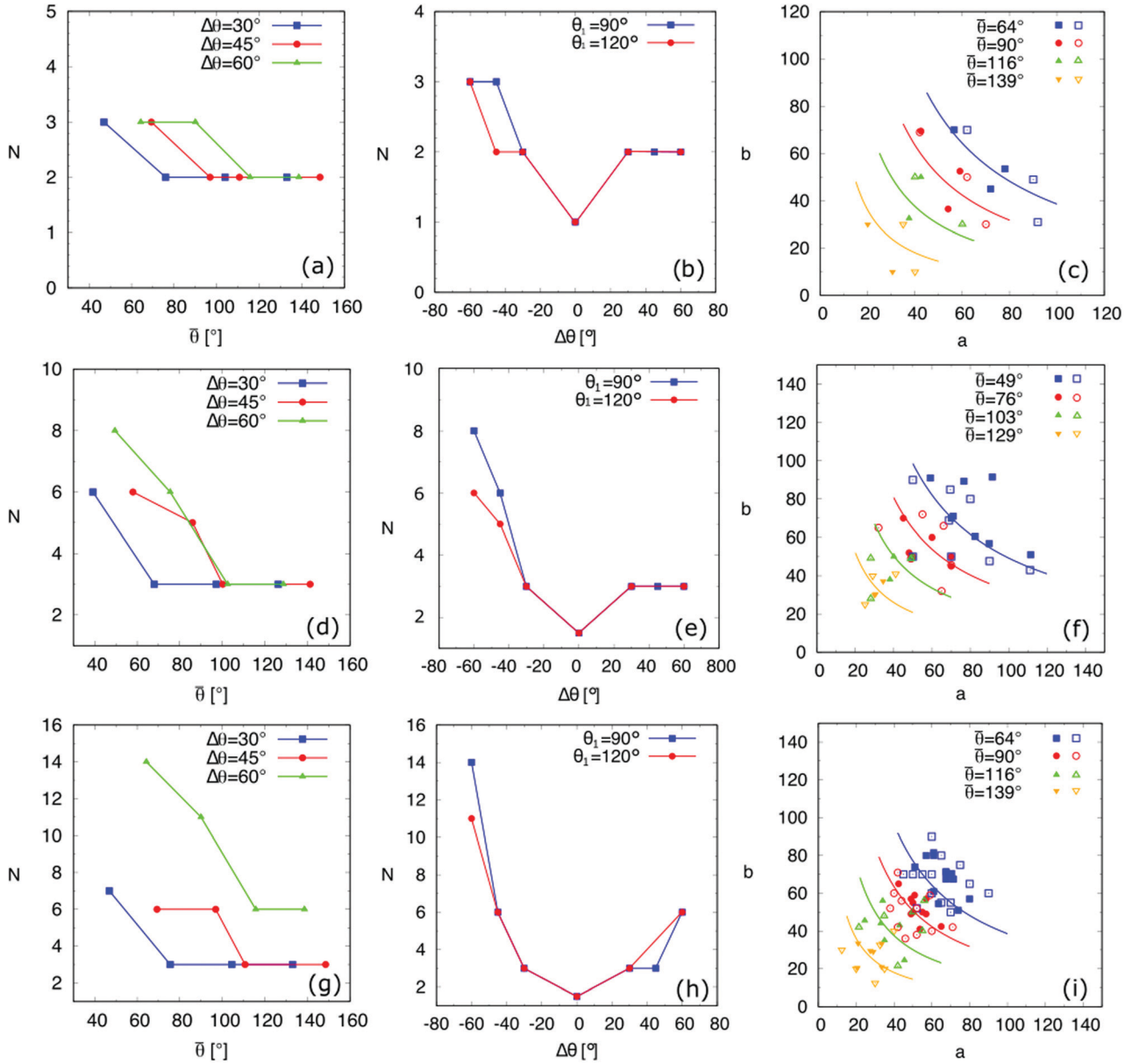

Fig. 8 The number and the morphologies of the equilibrated droplets on three typical chemically patterned surfaces in dependence of the contact angles. (a–c), (d–f), and (g–i) are for the striped, chocolate-patterned, and chessboard-patterned surfaces, respectively. (a) and (d) and (g), and (b) and (e) and (g) illustrate N *versus* $\bar{\theta}$ and $\Delta\theta$, respectively. Here, $\Delta\theta$ varies from -60° to 60°, which is achieved by fixing θ_1 (*e.g.* $\theta_1 = 90^\circ, 120^\circ$) and changing θ_2. (c), (f), and (i) depict the equilibrated droplet morphologies with different average contact angles predicted by PF simulations (filled symbols), in comparison with the energy-map model (hollow symbols) and the modified CB model (solid curves).

observation is due to the relatively small contact area resulting from a high value of $\bar{\theta} \geq 100^\circ$. The latter one is as a result of the high density of the discontinuous lines, which gives rise to a higher chance of pinning. For the striped and chocolate patterned surfaces, although the pinning effect becomes stronger with an increase in $\Delta\theta$ when $\Delta\theta > 0$, the number of pinning lines is not as high as the one for the chessboard pattern, when the size of the droplets is comparable with the characteristic length. In contrast, for the chessboard pattern, the high density of discontinuous lines facilitates the occurrence of more equilibrated shapes when the pinning effect is reinforced with a rise in $\Delta\theta$. From the relations N *vs.* $\bar{\theta}$ and N *vs.* $\Delta\theta$, we should set low values of $\bar{\theta}$ as well as high values of $|\Delta\theta|$ to obtain more equilibrated droplets, and *vice versa*.

Fig. 8(c), (f) and (i) describe the values (a,b) of equilibrated droplets from the PF simulations (filled symbols) and the energy landscape model (hollow symbols) for different $\bar{\theta}$. These results are compared with the modified CB model (solid curves). As $\bar{\theta}$ decreases, for droplets with the same size, the contact area tends to increase and therefore the curve $ab = \Psi(V_d;\bar{\theta})$ from the modified CB model translates upper right (see eqn (10)).

4.3 The ratio of the hydrophilic area to the hydrophobic area

Apart from changing θ_1 and θ_2, the average contact angle $\bar{\theta}$ can also be adjusted by tuning the area ratio of the hydrophilic area to the hydrophobic area while fixing the intrinsic contact angles on these two areas. In this part, we set the contact angles on the hydrophilic and hydrophobic areas as $\theta_1 = 60^\circ$ and $\theta_2 = 120^\circ$, respectively. As aforementioned, the area ratio of the hydrophilic area to the hydrophobic area is characterized by the parameter ν. For the chocolate patterned surfaces, we set ν = 1 : 1, 1 : 2, and 1 : 3 for the present investigation. To avoid repeated discussion of the similar wetting behaviors, the striped and chessboard-patterned surfaces will not be further discussed in this section.

For the chocolate-patterned surfaces with ν = 1 : 1, 1 : 2, and 1 : 3, the surface energy landscapes and the snapshots of the equilibrated droplets from the PF simulations are shown in Fig. 9(I), (II) and (III), respectively. The number N and the coordinates (a,b) of the local minima in the surface energy landscapes are both well corroborated by the simulations, as illustrated in Fig. 10(a) and (b), respectively. It is worth mentioning that we have converted the ratio ν into the average contact angle by using eqn (9). As ν decreases, *i.e.* $\bar{\theta}$ increases, the equilibrated droplet becomes spherical successively and N decreases. This finding coincides very well with the results shown in Fig. 8. The comparison between the simulation results, the energy landscape model, and the modified CB model is illustrated in Fig. 10(b), where sound agreement is obtained.

5 Summary and conclusions

In this study, we have shed light on the equilibrium morphologies of droplets on three typical chemically patterned surfaces. Because of the contact line pinning effect, the droplets reach different energy minimum states and thus achieve distinct equilibrium shapes. The number of equilibrated droplets and

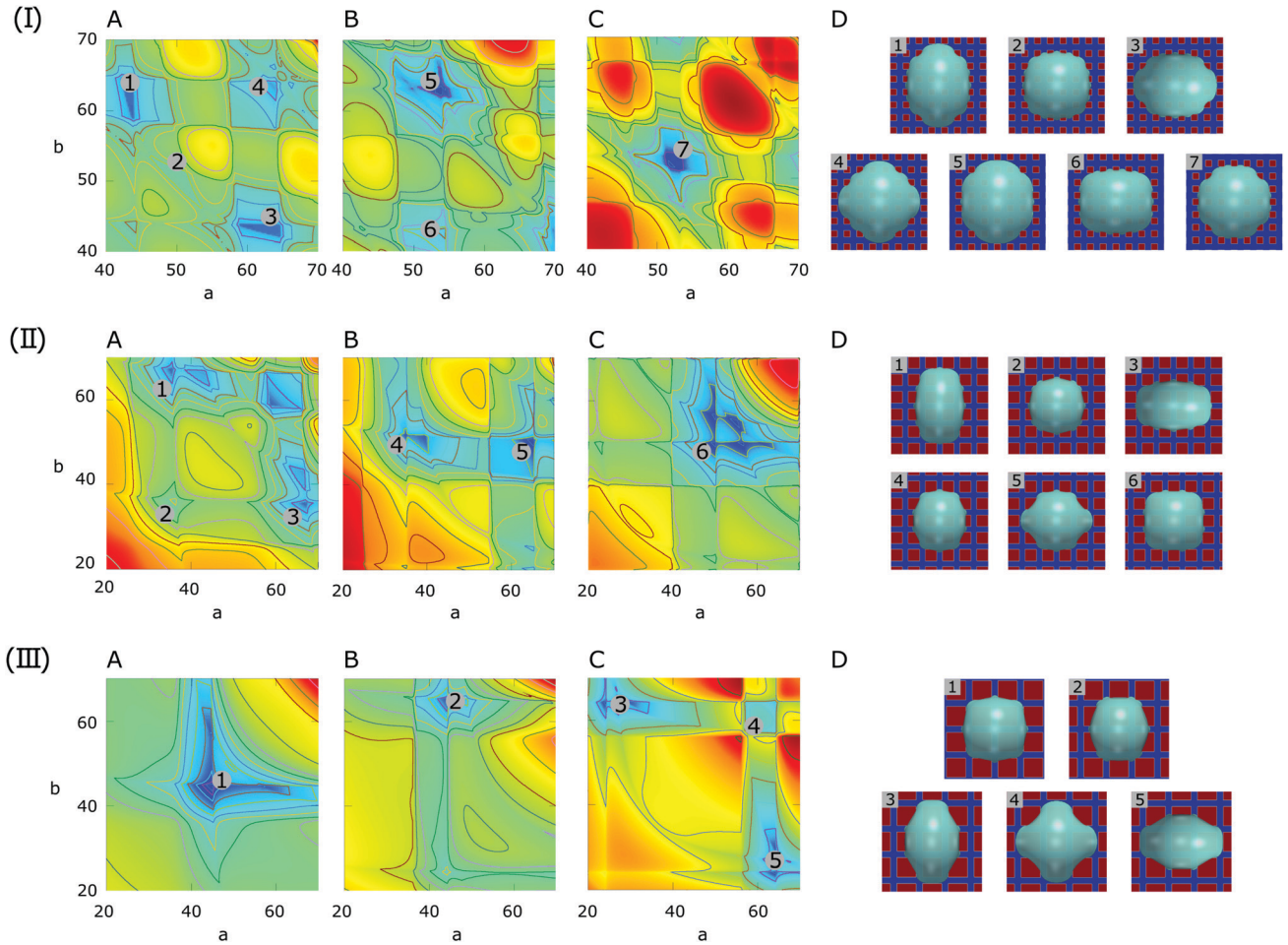

Fig. 9 Surface energy landscapes for droplets on chocolate patterned surfaces with different area fractions of hydrophilic and hydrophobic areas and corresponding snapshots of equilibrated droplets from PF simulations. The droplet size is set as R = 40. The chemical heterogeneities are described by $f_2(r_b,\varphi)$ in eqn (7) with γ_m = 0, γ_0 = 0.5, and ξ = 100. The ratios for (I) ν = 1 : 1, (II) ν = 1 : 2, and (II) ν = 1 : 3 correspond to (L = 20, λ = 0, χ = 0.55), (L = 30, λ = cos 60°, χ = 0.13), and (L = 40, λ = cos 45°, χ = 0.10), respectively. The energy minima are designated by different numbers, corresponding to the snapshots in (D) indicated with the same number. The surface energy landscapes for (A), (B) and (C) correspond to the droplet base center positions P_1, P_2 and P_3, respectively. (D) Snapshots of equilibrated droplets from PF simulations (blue: hydrophilic, red: hydrophobic).

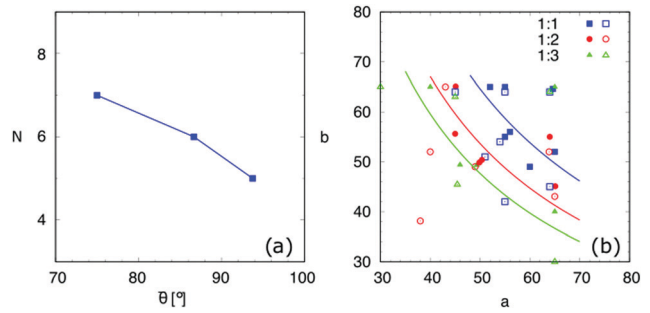

Fig. 10 (a) The number N of the equilibrium droplet shapes on chocolate patterned surfaces as a function of $\bar{\theta}$. (b) Equilibrium morphologies of droplets on chocolate patterned surfaces with different fractions of hydrophilic and hydrophobic areas predicted by PF simulations (filled symbols) compared with the energy landscape model (hollow symbols) and the modified CB model (solid curves).

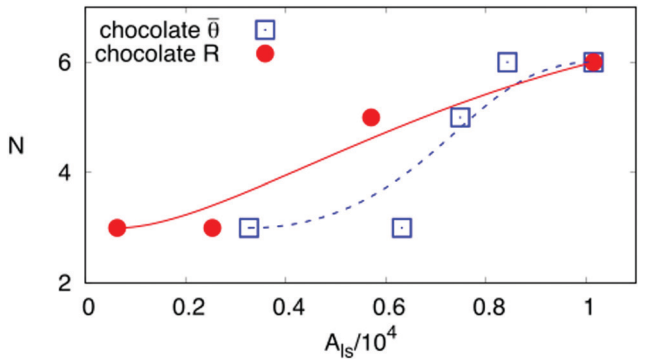

Fig. 11 Functional relation between N and A_{ls} for droplets on the chocolate-patterned surface. The hollow squares and filled circles depict two distinct cases, where A_{ls} is changed by setting different average contact angle $\bar{\theta}$ and droplet radius R values, respectively. The solid and dashed lines are the corresponding fitting curves.

the equilibrium morphologies are both dependent on the droplet sizes, contact angles, and the ratios of the hydrophilic area to the hydrophobic area. These influencing factors have been systematically discussed in this work. Our discussion is based on a combination of the surface energy landscape method with phase-field simulations. It has been shown that the analytical predictions obtained from the surface energy landscape approach are well consistent with the PF simulations. It is worth noting that in pure experiments or simulations, a number of tries are probably required to find all the equilibrium states with varying parameters and it is even likely that some equilibrium morphologies might be missed if the number of experimental samples is not sufficiently large. This demonstrates that the energy landscape model may be used as guidance for experiments and simulations without blind attempts.

Furthermore, we have noticed that the number of equilibrium droplet shapes for all three chemically patterned surfaces increases with the droplet volume. This tendency is due to the fact that an increase in droplet volume leads to an enlarged contact area between droplets and the substrates, so that the triple lines cross more energy discontinuous lines. On these discontinuous lines, the pinning effect occurs, resulting in more equilibrium shapes of droplets. Similarly, we have varied the contact angles on the hydrophilic and hydrophobic areas while fixing the droplet volume. We figured out that as the average contact angle decreases, *i.e.*, the substrate is globally relatively hydrophilic, the contact area between the droplet and substrate increases, which leads to a rise in the number of equilibrated states. To sum up, the increase in the volume or the decrease in the average contact angle engenders more equilibrium shapes of droplets. The average contact angles can be controlled either by changing the intrinsic contact angles on the hydrophilic and hydrophobic areas or the area ratio of these two components. It should be noticed that although both decreasing average contact angle and increasing volume lead to a large droplet–substrate contact area and thus facilitate more equilibrium states, a universal behavior for the number of equilibrium states N *versus* contact area A_{ls} does not exist. In Fig. 11, we plot the functional relation between N and A_{ls} for droplets on the chocolate-patterned surface. Here, different A_{ls} values are obtained by changing the average contact angle $\bar{\theta}$ (hollow squares) or droplet radius R (filled circles). As A_{ls} increases, N rises. Although the tendencies are similar between these two curves, the quantities of the equilibrium states for the same A_{ls} are not always the same. This reveals that N is not uniquely dependent on A_{ls}. Other aspects such as the pinning force or droplet height may also have an important role for the stability analysis of the droplets. Given the limit of the content, these factors will not be further discussed.

We have further investigated the morphological properties of the equilibrated droplets on different patterned surfaces. For a certain chemically patterned surface, the surface energy landscape method in combination with the PF simulations has been adopted to find the possible equilibrium shapes of droplets. These results have been compared with the modified CB model proposed in this work. It has been shown that the simulation results coincide with those of the modified CB model. This demonstrates that the proposed modified CB model is robust and able to accurately delineate the droplet shapes, especially the base area. Therefore, the classical CB model has been successfully extended to be able to predict the equilibrium droplet shapes, which are not necessarily in the shape of a spherical cap. The comprehensive predictions of the droplet shapes in this work are of significant importance for applications of droplet manipulation and the findings open a promising avenue for a delicate control of droplet formation as well as for the design of functional surfaces.

It should be emphasized that our model can be easily further extended to other chemically patterned surfaces whose heterogeneities are symmetric. In the present work, we have assumed that the droplet has the form of a quasi-spherical cap with an elliptical contact baseline on the substrate. However, it is beyond the validity of our model if the chemical pattern is extremely complex, where the droplet shapes become asymmetric.

Conflicts of interest

There are no conflicts to declare.

Acknowledgements

The authors gratefully acknowledge funding of the research through the Gottfried-Wilhelm Leibniz prize NE 822/31-1 of the German research foundation (DFG). Aspects of modelling wetting behaviour on a structured surface, integrated in the present manuscript, have been discussed within the VirtMat project of the Helmholtz association. The authors acknowledge support by the state of Baden-Württemberg through bwHPC.

Notes and references

1 J. Z. Wang, Z. H. Zheng, H. W. Li, W. T. S. Huck and H. Sirringhaus, *Nat. Mater.*, 2004, **3**, 171.
2 M. Singh, H. M. Haverinen, P. Dhagat and G. E. Jabbour, *Adv. Mater.*, 2010, **22**, 673–685.
3 C. Rascón, A. O. Parry and D. G. Aarts, *Proc. Natl. Acad. Sci. U. S. A.*, 2016, **113**, 12633–12636.
4 Y. Zheng, J. Cheng, C. Zhou, H. Xing, X. Wen, P. Pi and S. Xu, *Langmuir*, 2017, **33**, 4172–4177.
5 J. K. Park and S. Kim, *Lab Chip*, 2017, **17**, 1793–1801.
6 H. Geng, J. Feng, L. M. Stabryla and S. K. Cho, *Lab Chip*, 2017, **17**, 1060–1068.
7 R. D. Tilton, C. R. Robertson and A. P. Gast, *Langmuir*, 1991, **7**, 2710–2718.
8 S. Devineau, M. Anyfantakis, L. Marichal, L. Kiger, M. Morel, S. Rudiuk and D. Baigl, *J. Am. Chem. Soc.*, 2016, **138**, 11623–11632.
9 B. K. Park, D. Kim, S. Jeong, J. Moon and J. S. Kim, *Thin Solid Films*, 2007, **515**, 7706–7711.
10 Q. Liu and M. Orme, *J. Mater. Process. Technol.*, 2001, **115**, 271–283.
11 E. Ueda, F. L. Geyer, V. Nedashkivska and P. A. Levkin, *Lab Chip*, 2012, **12**, 5218–5224.
12 W. Feng, L. Li, E. Ueda, J. Li, S. Heißler, A. Welle, O. Trapp and P. A. Levkin, *Adv. Mater. Interfaces*, 2014, **1**, 1400269.
13 D. Tian, Y. Song and L. Jiang, *Chem. Soc. Rev.*, 2013, **42**, 5184–5209.
14 R. Raj, R. Enright, Y. Zhu, S. Adera and E. N. Wang, *Langmuir*, 2012, **28**, 15777–15788.
15 R. Raj, S. Adera, R. Enright and E. N. Wang, *Nat. Commun.*, 2014, **5**, 4975.
16 P. Zhu, T. Kong, X. Tang and L. Wang, *Nat. Commun.*, 2017, **8**, 15823.
17 D. P. Regan and C. Howell, *Curr. Opin. Colloid Interface Sci.*, 2019, **39**, 137–147.
18 M. Brinkmann and R. Lipowsky, *J. Appl. Phys.*, 2002, **92**, 4296–4306.
19 H. Kusumaatmaja and J. M. Yeomans, *Langmuir*, 2007, **23**, 6019–6032.
20 A. Cassie, *Discuss. Faraday Soc.*, 1948, **3**, 11–16.
21 E. Bormashenko, Y. Bormashenko, G. Whyman, R. Pogreb and O. Stanevsky, *J. Colloid Interface Sci.*, 2006, **302**, 308–311.
22 H. Y. Erbil and C. E. Cansoy, *Langmuir*, 2009, **25**, 14135–14145.
23 Y. Kwon, S. Choi, N. Anantharaju, J. Lee, M. Panchagnula and N. A. Patankar, *Langmuir*, 2010, **26**, 17528–17531.
24 A. Marmur and E. Bittoun, *Langmuir*, 2009, **25**, 1277–1281.
25 G. McHale, *Langmuir*, 2007, **23**, 8200–8205.
26 L. Gao and T. J. McCarthy, *Langmuir*, 2007, **23**, 3762–3765.
27 G. Whyman, E. Bormashenko and T. Stein, *Chem. Phys. Lett.*, 2008, **450**, 355–359.
28 A. Milne and A. Amirfazli, *Adv. Colloid Interface Sci.*, 2012, **170**, 48–55.
29 X. Xu and X. Wang, *Colloid Polym. Sci.*, 2013, **291**, 299–306.
30 J. Carmeliet, L. Chen, Q. Kang and D. Derome, *Langmuir*, 2017, **33**, 6192–6200.
31 D. Xia, L. M. Johnson and G. P. López, *Adv. Mater.*, 2012, **24**, 1287–1302.
32 H. Kusumaatmaja, J. Léopoldès, A. Dupuis and J. M. Yeomans, *Europhys. Lett.*, 2006, **73**, 740–746.
33 O. Bliznyuk, E. Vereshchagina, E. S. Kooij and B. Poelsema, *Phys. Rev. E: Stat., Nonlinear, Soft Matter Phys.*, 2009, **79**, 1–6.
34 D. Ferraro, C. Semprebon, T. Tóth, E. Locatelli, M. Pierno, G. Mistura and M. Brinkmann, *Langmuir*, 2012, **28**, 13919–13923.
35 R. David and A. W. Neumann, *Colloids Surf., A*, 2012, **393**, 32–36.
36 H. P. Jansen, O. Bliznyuk, E. S. Kooij, B. Poelsema and H. J. Zandvliet, *Langmuir*, 2012, **28**, 499–505.
37 H. P. Jansen, K. Sotthewes, C. Ganser, H. J. Zandvliet, C. Teichert and E. S. Kooij, *Langmuir*, 2014, **30**, 11574–11581.
38 S. Varagnolo, V. Schiocchet, D. Ferraro, M. Pierno, G. Mistura, M. Sbragaglia, A. Gupta and G. Amati, *Langmuir*, 2014, **30**, 2401–2409.
39 H. P. Jansen, K. Sotthewes, H. J. Zandvliet and E. S. Kooij, *Appl. Surf. Sci.*, 2016, **361**, 122–132.
40 C. Honisch, T.-S. Lin, A. Heuer, U. Thiele and S. V. Gurevich, *Langmuir*, 2015, **31**, 10618–10631.
41 X. Cai, H. Marschall, M. Wörner and O. Deutschmann, *Chem. Eng. Technol.*, 2015, **38**, 1985–1992.
42 Y. Yu, Q. Li, C. Q. Zhou, P. Zhou and H. Yan, *Appl. Therm. Eng.*, 2017, **127**, 1346–1354.
43 R. Lipowsky, M. Brinkmann, R. Dimova, T. Franke, J. Kierfeld and X. Zhang, *J. Phys.: Condens. Matter*, 2005, **17**, S537.
44 M. Brinkmann, J. Kierfeld and R. Lipowsky, *J. Phys. A: Math. Gen.*, 2004, **37**, 11547.
45 P. Lenz and R. Lipowsky, *Phys. Rev. Lett.*, 1998, **80**, 1920.
46 H. Gau, S. Herminghaus, P. Lenz and R. Lipowsky, *Science*, 1999, **283**, 46–49.
47 R. Lipowsky, *Curr. Opin. Colloid Interface Sci.*, 2001, **6**, 40–48.
48 Y. Yan and Y. Zu, *J. Comput. Phys.*, 2007, **227**, 763–775.
49 A. Gupta and R. Kumar, *Comput. Phys. Commun.*, 2011, **10**, 767–784.
50 U. Thiele, L. Brusch, M. Bestehorn and M. Bär, *Eur. Phys. J. E: Soft Matter Biol. Phys.*, 2003, **11**, 255–271.
51 S. O'brien and L. Schwartz, *Encycl. Surf. Colloid Sci.*, 2002, **1**, 5283–5297.
52 J. W. Cahn, *J. Chem. Phys.*, 1965, **42**, 93–99.
53 U. Thiele, *Eur. Phys. J. E: Soft Matter Biol. Phys.*, 2003, **12**, 409–416.
54 J. Shen and X. Yang, *Discrete Contin. Dyn. Syst.*, 2010, **28**, 1669–1691.

55 R. Xie, A. Karim, J. F. Douglas, C. C. Han and R. A. Weiss, *Phys. Rev. Lett.*, 1998, **81**, 1251.
56 U. Thiele, M. G. Velarde and K. Neuffer, *Phys. Rev. Lett.*, 2001, **87**, 016104.
57 P. Beltrame, E. Knobloch, P. Hänggi and U. Thiele, *Phys. Rev. E: Stat., Nonlinear, Soft Matter Phys.*, 2011, **83**, 016305.
58 B. Nestler, F. Wendler, M. Selzer, B. Stinner and H. Garcke, *Phys. Rev. E: Stat., Nonlinear, Soft Matter Phys.*, 2008, **78**, 011604.
59 D. M. Anderson, G. B. McFadden and A. A. Wheeler, *Annu. Rev. Fluid Mech.*, 1998, **30**, 139–165.
60 J. J. Feng, C. Liu, J. Shen and P. Yue, *An energetic variational formulation with phase field methods for interfacial dynamics of complex fluids: advantages and challenges*, Springer, 2005, pp. 1–26.
61 Y. Wu, F. Wang, M. Selzer and B. Nestler, *Phys. Rev. E*, 2019, **100**, 041102.
62 M. Ben Said, M. Selzer, B. Nestler, D. Braun, C. Greiner and H. Garcke, *Langmuir*, 2014, **30**, 4033–4039.
63 K. Schweigler, M. Ben Said, S. Seifritz, M. Selzer and B. Nestler, *Int. J. Heat Mass Transfer*, 2017, **105**, 655–663.
64 Y. Wu, F. Wang, M. Selzer and B. Nestler, *Langmuir*, 2019, **35**, 8500–8516.
65 H. Kusumaatmaja, J. Leopoldes, A. Dupuis and J. Yeomans, *EPL*, 2006, **73**, 740.
66 A. Badillo, *Phys. Rev. E: Stat., Nonlinear, Soft Matter Phys.*, 2015, **91**, 033005.
67 F. Diewald, C. Kuhn, M. Heier, M. Horsch, K. Langenbach, H. Hasse and R. Müller, *PAMM*, 2017, **17**, 501–502.
68 H. Garcke, B. Nestler, B. Stinner and F. Wendler, *Math. Models Methods Appl. Sci.*, 2008, **18**, 1347–1381.
69 D. Jacqmin, *J. Fluid Mech.*, 2000, **402**, 57–88.
70 A. Carlson, M. Do-Quang and G. Amberg, *Phys. Fluids*, 2009, **21**, 121701.